14   Computer Assisted Physics

C. Bersier (since May 01), P. F. Meier, E. Olbrich,
S. Pliberšek (until Sept. 01), S. Renold, J. Schneider (until Aug. 01) and Y. Shen

In this report, we want to concentrate on the following research topics:

- Interpretation of the properties of high temperature superconductivity materials using spin-polarised theoretical methods.

  We selectively report on the differences of electric field gradients derived from first-principles and point-ion calculations (14.1.1), on the calculation of the microscopic structure of $YBa_2Cu_3O_7$, in particular the study of electric field gradients and hyperfine couplings (14.1.2), and on an investigation of the differences in the electronic structures of La_2CuO_4 and $Sr_2CuO_2Cl_2$ (14.1.3).

- Non-linear dynamical study with particular reference to time series analysis of electroencephalograms.

  This involves collaboration with two groups of the Medical Faculty and we jointly present results of time series analysis of epilepsy EEG.

14.1   Electronic structure of high-T_c materials

14.1.1   Electric field gradients from first-principles and point-ion calculations
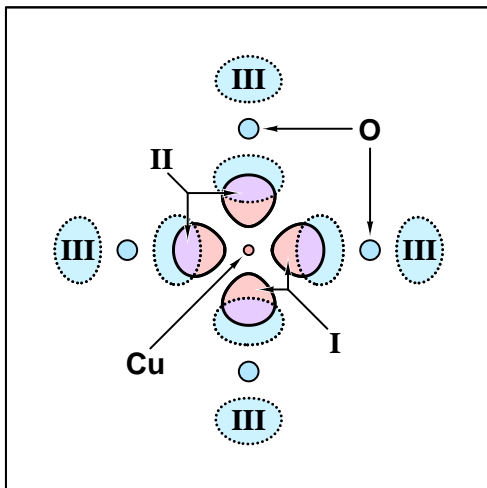

Figure 14.1: *Schematic illustration of the contributions I to III to electron densities for a molecular orbital in a CuO_4 cluster. In the centre there is a Cu atom which is surrounded by four neighbouring O atoms. To simplify matters we have drawn only the regions I of the central Cu d-electrons circumscribed by solid curves, the regions III of the oxygen p-electrons circumscribed by dotted curves, and the overlap regions II of d- and p-electrons.*

Point-ion models have been extensively used to determine "hole numbers" at copper and oxygen sites in high-temperature superconducting cuprate compounds from measured nuclear quadrupole frequencies. We embarked on a project to assess the reliability of point-ion models to predict electric field gradients accurately and also to test the validity of the implicit assumption that the values can be calculated from the "holes" rather than the total electronic structure. The latter assumption was readily shown to have a very limited range of applicability.

First-principles cluster calculations using basis sets centred on the nuclei enabled us to determine the charge and spin density distribution in the CuO_2-plane. We analysed in detail the contributions to the electric field gradients and the magnetic hyperfine couplings. In

particular we partitioned the contributions into regions I, II, and III (see Fig. 14.1). The regional partition I comprises all contributions from on-site basis functions (the given example illustrates the electron density attributed to the atomic $3d$ wave functions). Contributions arising from both on-site ($3d$) and off site (oxygen $2p$) basis functions belong to region II. Region III contains no reference to the on-site basis functions.

This partitioning scheme was chosen in an attempt to find a correlation with the most commonly used point-ion model, the Sternheimer equation: $V_{ii} = (1-R)V_{ii}^{local} + (1-\gamma)V_{ii}^{lattice}$ which depends on the two parameters R and γ. Our most optimistic objective was to find expressions for these parameters, which would improve our understanding of them, but although estimates of the R parameter were encouraging the method used to obtain the γ parameter indicated that the two parameters may not be independent. The problem seems to stem from the covalently bonded nature of the CuO$_2$-planes in these structures which severely questions using the Sternheimer equation for such crystals, since its derivation is heavily reliant on the application of perturbation theory to predominantly ionic structures. Furthermore it was shown that the complementary contributions of electrons and holes in an isolated ion cannot be applied to estimates of electric field gradients at copper and oxygen nuclei in cuprates. For more details, see Ref. [1].

14.1.2 First-principles calculation of electric field gradients and hyperfine couplings in YBa$_2$Cu$_3$O$_7$

YBa$_2$Cu$_3$O$_7$ is a high temperature superconducting material which has a lower symmetry than La$_2$CuO$_4$ which has been studied before. The local electronic structure of YBa$_2$Cu$_3$O$_7$ was calculated using first-principles cluster methods. Several clusters of differing size, embedded in an appropriate background potential, were investigated. The electric field gradients at the copper and oxygen sites were determined and compared to previous theoretical calculations and experiments. Spin polarised calculations with different spin multiplicities have enabled a detailed study of the spin density distribution to be made and a simultaneous determination of magnetic hyperfine coupling parameters. The contributions from on-site and transferred hyperfine fields have been disentangled. The mechanism of the spin transfer from the two neighbouring Cu^{2+}-ions to the oxygen is illustrated in Fig. 14.2 where the difference $D(\vec{r})$
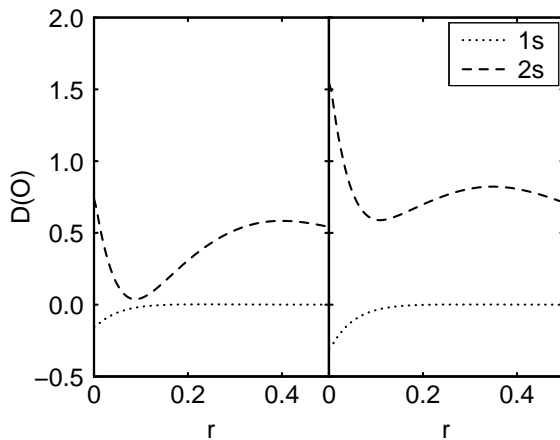

Figure 14.2: *Radial dependence (along bond direction in units of a_B) of D (in a_B^{-3}) subdivided into contributions from MOs with mainly 1s and 2s AO character at a planar oxygen nucleus for the small cluster $CuO_5/Cu_5Y_{12}Ba_{12}$ with one Cu^{2+} neighbour (left panel) and for the large cluster $Cu_5O_{21}/Cu_{13}Y_{12}Ba_{12}$ with two Cu^{2+} neighbours (right panel).*

between spin-up, $|\psi^\uparrow|^2$, and spin-down, $|\psi^\downarrow|^2$, densities, around the oxygen nucleus is shown. In the left panel of Fig. 14.2, the spin density transferred from a single copper ion is shown, subdivided into contributions of mainly 1s and 2s character around the oxygen. On the right panel, the oxygen is surrounded by two nearest neighbour copper ions. The value of the

contact term at $(r = 0)$ is now $D = 1.56$ which corresponds to twice the value in the left panel.

A detailed analysis (see Ref. [2]) has shown that the transferred spin densities at the oxygen essentially are due to nearest neighbour copper ions only with marginal influence of ions further away. This implies that the variant temperature dependencies of the planar copper and oxygen NMR spin-lattice relaxation rates are only compatible with commensurate anti-ferromagnetic correlations.

Furthermore, the theoretical hyperfine parameters have been compared with those derived from experimental data. It was found that the on-site hyperfine field A^c at the copper nucleus perpendicular to the CuO_2-plane is not cancelled by $4B$, the field transferred from the four nearest neighbour ions. Such an incidental correlation, however, is required to explain the observed temperature independence of the Cu magnetic shift with field parallel to the c-axis.

14.1.3 La_2CuO_4 versus $Sr_2CuO_2Cl_2$, similarities and differences in electronic structure

The structural and magnetic properties of $Sr_2CuO_2Cl_2$ are almost identical to the ones in La_2CuO_4 except: (i) the La_2CuO_4 crystal structure shows a phase transition from tetragonal to orthorhombic while the substance with chlorine at the apex positions remains tetragonal; (ii) La_2CuO_4 can easily be doped and becomes superconducting, while $Sr_2CuO_2Cl_2$ can only be doped with difficulty. Since we had already studied the electronic structure of La_2CuO_4 in detail we embarked on a similar project to investigate $Sr_2CuO_2Cl_2$. Effectively we are studying the changes introduced by replacing the axial oxygen ions in La_2CuO_4 with chlorine ions, the strontium counter ions simply maintaining the correct charge balance, in an attempt to rationalise the differences qualitatively. So far two clusters have been investigated: (a) a small octahedral-like cluster, CuO_4Cl_2 and (b) the cluster $Cu_5O_{16}Cl_{10}$ made up of effectively five CuO_4Cl_2 octahedra (see Fig. 14.3.).
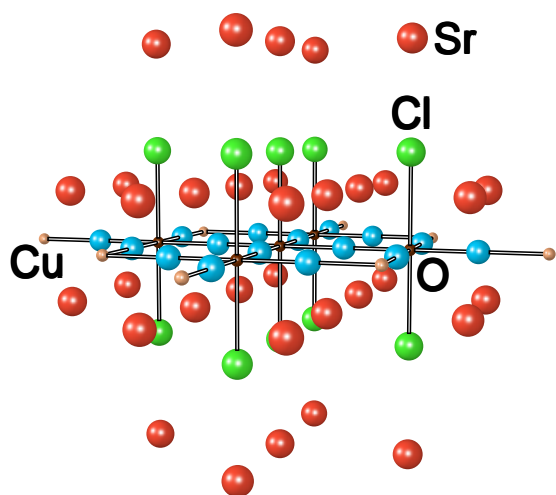

Figure 14.3: *The $Cu_5O_{16}Cl_{10}$ cluster with 5 Cu (black) and 16 O atoms in the CuO_2 plane and 10 apical Cl atoms. These atoms have been provided with basis sets. In addition 34 Sr^{2+} atoms and 8 Cu^{2+} atoms are represented with pseudopotentials.*

Since spin-polarised calculations have been carried out the spin-up molecular spin-polarised orbital (MSO) energies are distinct from the spin-down MSO energies. In Fig. 14.4 the calculated orbitals with energies in an interval of 7 eV below the Fermi energy are plotted with solid bars for spin-up MSOs and dotted bars for spin-down MSOs. The highest occupied MSO (HOMO) is an anti-bonding orbital predominantly between Cu $3d_{x^2-y^2}$ and the four planar O $2p_\sigma$ AOs, probably best interpreted as non-bonding or at most weakly anti-bonding.
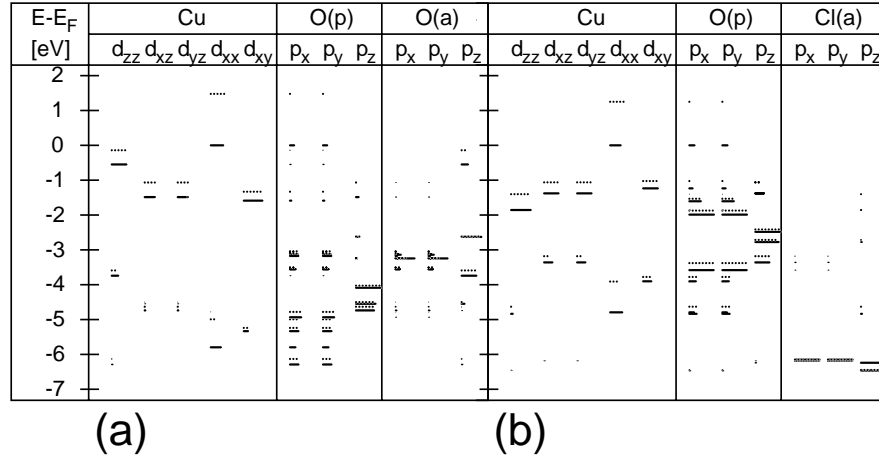
Figure 14.4: *Energies of the highest occupied MSOs in (a) the CuO_6/Cu_4La_{10}-cluster and (b) in the CuO_4Cl_2/Cu_4Sr_{10}-cluster with contributions of the individual AOs. The length of the bar is proportional to the square of the expansion coefficient of the MSO into the corresponding AOs. Spin-up (spin-down) orbitals are denoted by solid (dotted) bars.*

This is occupied by a spin-up electron but the corresponding spin-down anti-bonding MSO (1.3 eV higher) is unoccupied and is referred to as the lowest unoccupied MSO (LUMO). Also in Fig. 14.4 the composition of each MSO in terms of the more important atomic orbitals is indicated.

Just below these MSOs are MSOs which are interpreted to be the anti-bonding combinations of the Cu $3d_{3z^2-r^2}$ and apical O $2p_z$ orbitals. These are followed at energies around -1.5 eV by MSOs that can be formed as anti-bonding combinations with the three other Cu $3d$ AOs, thought to be effectively non-bonding. Deeper in energy, between -2.6 and -4.4 eV, are the MSOs that are composed of oxygens only without contributions from Cu. They comprise the $2p_z$ AOs of the planar oxygens and the $2p_x$ and $2p_y$ of the apex oxygens. The MSOs at lower energies are bonding combinations between the Cu $3d$ and the O $2p$ AOs.

The $3d_{3z^2-r^2}$ orbital participates at slightly lower orbital energies than the $d_{x^2-y^2}$ orbital in La_2CuO_4 as expected for the crystal field of a distorted octahedron extended along the z-axis. The corresponding $3d_{3z^2-r^2}$ orbital in the $Sr_2CuO_4Cl_2$ compound is lowered significantly in energy, even below the $3d_{xy}$, $3d_{yz}$ and $3d_{xz}$ orbital energies, which is characteristic of a square planar complex. The chlorine ions are so far removed that their influence on the crystal field is now relatively small. This may account for the observation that this crystal behaves like a 'perfect' two-dimensional anti-ferromagnet. This is to be contrasted with the occupied orbitals of the La compound which involve the $3d_{3z^2-r^2}$ orbital as well as the apical oxygen orbitals. The planar anti-ferromagnetic behaviour is clearly disturbed by this extra delocalisation in the z-direction.

14.2   Time series analysis of epilepsy EEG

Our research on nonlinear time series analysis of electroencephalograms (EEG) is continuing, a project which is conducted in collaboration with the institute of pharmacology and toxicology and the neurological clinic. Our studies have concentrated on two main aspects: (i) developing a general dynamical model of the EEG and, from the results of an EEG analysis, (ii) understanding the processes of sleep and epilepsy and how they interact.

Our investigations were focused on non-linearity in the intracranial EEG of patients suffering from epilepsy. We addressed both the temporal evolution of non-linearity in course of sleep and the spatial distribution of non-linearity in the brain. Non-linearity can be analysed by comparing the dimensional complexity (DC) of the original EEG data with those of surrogate data, which show the same linear properties as the original data but are otherwise random. The null-hypothesis that EEG signals could be generated by linear processes can be rejected with 95% probability, if the measure for significance of surrogate data test S, which is defined by

$$S = \frac{|\langle DC^{\mathrm{surr}}\rangle - DC|}{\sigma(DC^{\mathrm{surr}})},$$
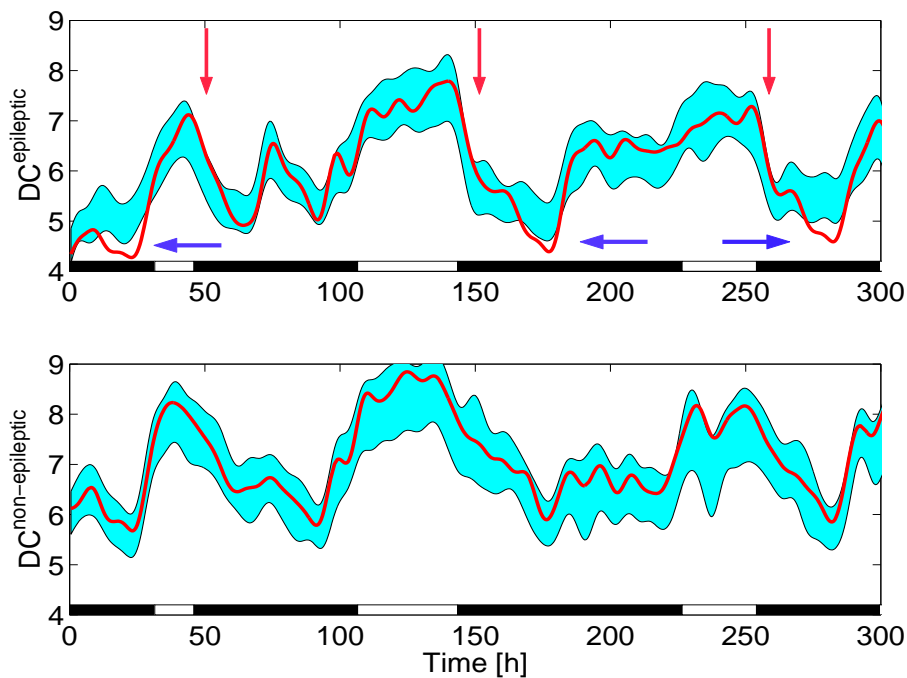
is larger than the threshold value two.

Figure 14.5: *Time courses of dimensional complexity DC for the intracranial sleep EEG of one epilepsy patient (for details see text).*
Upper panel: The DC-values for the original EEG channel derived from the epileptic hemisphere are represented by the red curve (steepest descents are marked by red arrows), whereas those for surrogate data are displayed by the cyan shaded area corresponding to $\langle DC^{surr}\rangle \pm 2 \times \sigma(DC^{surr})$. The blue arrows point out prominent non-linearity.
Lower panel: as for the upper panel but for the EEG channel from the healthy hemisphere.
At the bottom of each panel, a white bar indicates the occurrence of REM sleep.

In Fig. 14.5 we compare the time courses of the DC (red curves) for two intracranial EEG channels of one patient. One EEG is derived from the epileptic hemisphere (upper panel) and the other one from the healthy hemisphere (lower panel). To detect non-linearity in both EEG channels, the DC-values for the surrogate data are also displayed in terms of the blue area corresponding to $\langle DC^{\mathrm{surr}}\rangle \pm 2 \times \sigma(DC^{\mathrm{surr}})$. Firstly, we observe that the cyclic changes of DC-values for both channels coincide to a large extent with the alternation of non-REM and REM sleep cycles. This means that the DC-values of intracranial EEG can reflect sleep intensity in the same way as those of scalp EEG. However, the DC-values of the channel in

the epileptic area decrease steeper during the transition from REM sleep to non-REM sleep than in the non-epileptic hemisphere shown in the lower panel. This is emphasised in Fig. 14.5 by the red arrows and can be explained by the occurrence of the abnormal slow-wave activity in the epileptic channel. Secondly, it is seen that for the epileptic channel the DC-curve of the original data deviates from the shaded area during three short episodes within non-REM sleep, which are denoted by the blue arrows in Fig. 14.5. Note that this deviation indicates prominent non-linearity. Since these non-linear signatures are observed only in the epileptic channel, we conclude that they reflect the epileptic activity only. Furthermore, we find that non-linearity emerges not in REM sleep but in the central part of non-REM sleep, where the DC-value reaches its minimum. Therefore, we suggest that sleep processes can promote epileptic activity.
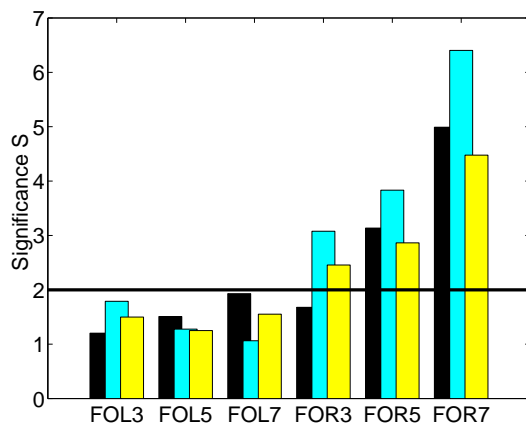

Figure 14.6: *The degree of nonlinearity for intracranial EEG recordings from a patient with temporal lobe epilepsy. Six bipolar derivations are shown: three from the left and three from the right. The different bars correspond to different recording conditions: sleep (black and turquoise) and awake (yellow). The horizontal line denotes the threshold alue S = 2 (for details see text).*

Now we turn our attention to the spatial distribution of non-linearity in the brain of patients suffering from epilepsy. The significance of surrogate data test S was used for quantifying non-linearity. Three intracranial recordings of one patient were analysed. For each recording we chose 6 artifact-free channels, three of them from the epileptic hemisphere (FOR3, FOR5 and FOR7) and the other three from the healthy hemisphere (FOL3, FOL5 and FOL7). The mean value of the S for each of these channels is displayed in Fig. 14.6. Firstly, we see that prominent non-linearity, i.e. the S-value larger than the threshold value two, occurs only in the channels from the epileptic hemisphere. Secondly, the S-values decrease gradually from FOR7 to FOR3 within the epileptic hemisphere. Since it is known that for this patient the epileptic focus is nearest to channel FOR7, we conclude that the degree of non-linearity in an EEG channel decreases with the increasing distance between the epileptic focus and the electrode from which this channel was derived. In summary, the degree of non-linearity we have used can describe epileptic activity in the intracranial EEG recording quantitatively.

References

[1] Electric field gradients from first-principles and point-ion calculations
    E. P. Stoll, T. A. Claxton, and P. F. Meier
    Phys. Rev. B, **65**, 064532-12 (2002)

[2] First-Principles Calculation of Electric Field Gradients and Hyperfine Couplings in YBa$_2$Cu$_3$O$_7$
    S. Renold, S. Pliberšek, E. P. Stoll, T. A. Claxton, and P. F. Meier
    Eur. Phys. J. B, **23**, 3-15 (2001)